1

Introduction

Electron beam scattering has had a long and distinguished history. Some of the essential physics was investigated even before the first electron microscope was built. The unsuspecting reader may find it surprising to come across familiar names such as Bethe, Bohr, Rutherford, Fermi and Mott in this book. While electron beam scattering is a mature theory its widespread use in electron microscopy measurements is arguably a more recent phenomenon. This is primarily due to two reasons. The first is the processing speed of modern computers; even a standard desktop computer can now produce useful results within a reasonable time and thankfully there are many software packages that take advantage of this. The second reason is the emergence of a new generation of electron microscopes that can resolve atom columns that are less than an angstrom apart, that have ~10 meV energy resolution or less for measuring vibronic modes and that can record events separated in time by femtoseconds. With such a wealth of new information there is a strong emphasis on extracting quantitative information about the sample. Electron beam scattering calculations are often indispensable for correct data interpretation.

Two examples help illustrate the advantages of combining experimental results with simulation. The first is using high angle annular dark field (HAADF) imaging in a scanning transmission electron microscope (STEM) to characterise the interface in an AlAs–GaAs superlattice (Robb and Craven, 2008; Robb *et al.,* 2012). Figure 1.1a shows the HAADF image of a [110]-oriented, epitaxial AlAs–GaAs superlattice acquired using an aberration corrected STEM. In this orientation the Group III–V elements are distributed as closely spaced (i.e. ~1.4 Å) atom column pairs or 'dumbbells'. The HAADF signal increases monotonically with

Electron Beam-Specimen Interactions and Simulation Methods in Microscopy,
First Edition. Budhika G. Mendis.

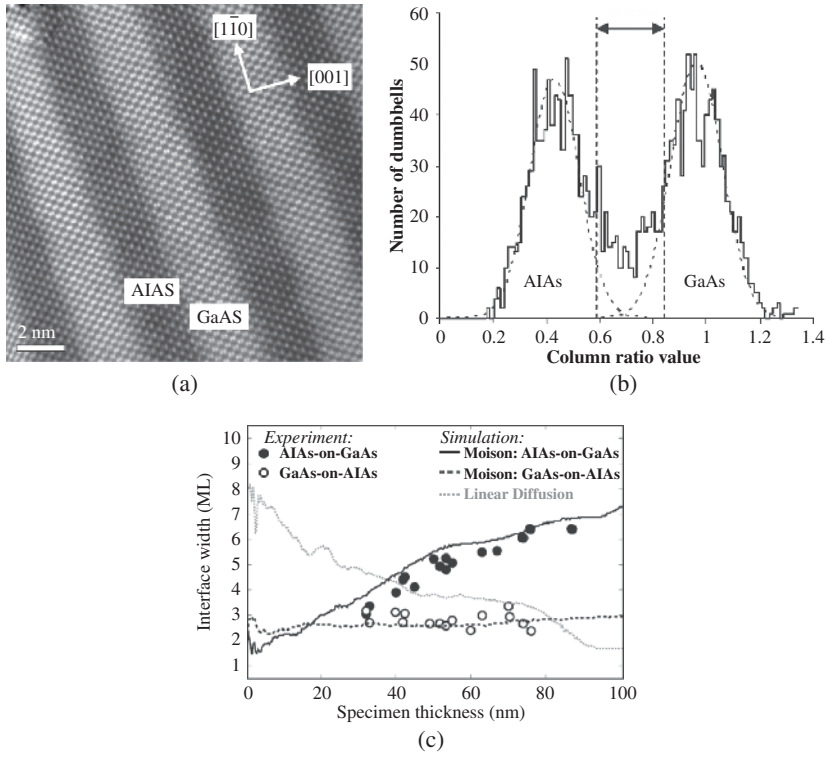

Figure 1.1 (a) HAADF STEM image of a [110]-oriented, AlAs–GaAs superlattice. The background subtracted column intensity ratio values for all dumbbells in (a) are shown in (b) as a histogram. (c) plots experimental and multislice simulated values for the AlAs–GaAs interface width, as defined from the column intensity ratio profile, as a function of specimen thickness. Supercells for the multislice simulation are constructed assuming a linear diffusion model and a more accurate diffusion model (Moison *et al.*, 1989) valid for the AlAs–GaAs system. Results are shown for superlattices grown on GaAs (labelled 'AlAs-on-GaAs') and AlAs (labelled 'GaAs-on-AlAs') substrates respectively. (a) and (b) From Robb and Craven (2008). Reproduced with permission; copyright Elsevier. (c) From Robb *et al*. (2012). Reproduced with permission; copyright Elsevier.

the atomic number of the scattering element, so that using AlAs dumbbells as an example, the intensity of an As column is larger than that of Al. Figure 1.1b is a histogram of the background subtracted column intensity ratio values for all dumbbells in Figure 1.1a. The two prominent peaks are due to dumbbells in 'bulk' AlAs and 'bulk' GaAs respectively. However, there are also intermediate values for the column intensity ratio (arrowed region in Figure 1.1b) and further analysis reveals these to be due to dumbbells located at the AlAs–GaAs interface region (Robb and Craven, 2008). An interface 'width' can be defined based on the 5–95% variation in column intensity ratio across the interface. The interface

width is found to be independent of the specimen thickness for superlattices grown on an AlAs substrate, but not on GaAs substrate.

It is not clear if the interface width is due to chemical inter-diffusion, electron beam spreading within the sample or interfacial roughness. This can, however, be tested by constructing supercells representing the different scenarios and performing multislice simulations (Chapter 3). Figure 1.1c shows the simulated results for chemical diffusion. The interface width, as deduced from the column intensity ratio values, is plotted as a function of specimen thickness for a linear composition profile and a more realistic diffusion model valid for the AlAs–GaAs system (Moison *et al.,* 1989). The latter accurately reproduces the experimental results, suggesting diffusion as a likely candidate. In fact, simulations for a saw tooth-shaped and smooth interface did not agree with experiment, so that interfacial roughness and beam spreading have only a secondary effect on the measurement (Robb *et al.,* 2012).

The second example is the use of electron energy loss spectroscopy (EELS) to extract the local electronic density of states for a silicon dopant atom in graphene (Ramasse *et al.,* 2013). As illustrated in Figure 1.2a, the silicon atom can be incorporated either through direct substitution (i.e. threefold coordination) or as a fourfold coordinated atom in defect regions of the graphene sheet. The dopant atom can be readily identified using HAADF imaging in an aberration corrected STEM, taking advantage of the higher atomic number of silicon compared to carbon. The solid lines in Figure 1.2b are the Si $L_{2,3}$-EELS edges measured from the two different dopant atom configurations. Owing to the nature of inelastic scattering (Chapter 5) the shape of the EELS spectrum is governed by the angular momentum resolved unoccupied density of electronic states. The filled spectra in Figure 1.2b are the results obtained from density functional theory simulation. There is excellent agreement between theory and experiment for the fourfold coordinated atom. For the threefold coordinated atom, however, accurate results are only obtained if it is assumed that the silicon dopant atom is displaced out of the graphene sheet (Figure 1.2a). This can be justified by the slightly longer Si–C bond length compared to graphene (note that the structure was relaxed to its lowest energy configuration prior to EELS simulation; Ramasse *et al.,* 2013). The out-of-plane displacement of the silicon atom is not evident in the HAADF image and was only revealed through a careful quantitative analysis of the EELS result with the aid of simulation.

1.1 ORGANISATION AND SCOPE OF THE BOOK

There are many ways to simulate electron beam scattering. Although the fundamental physics is unchanged, there are differences in the manner

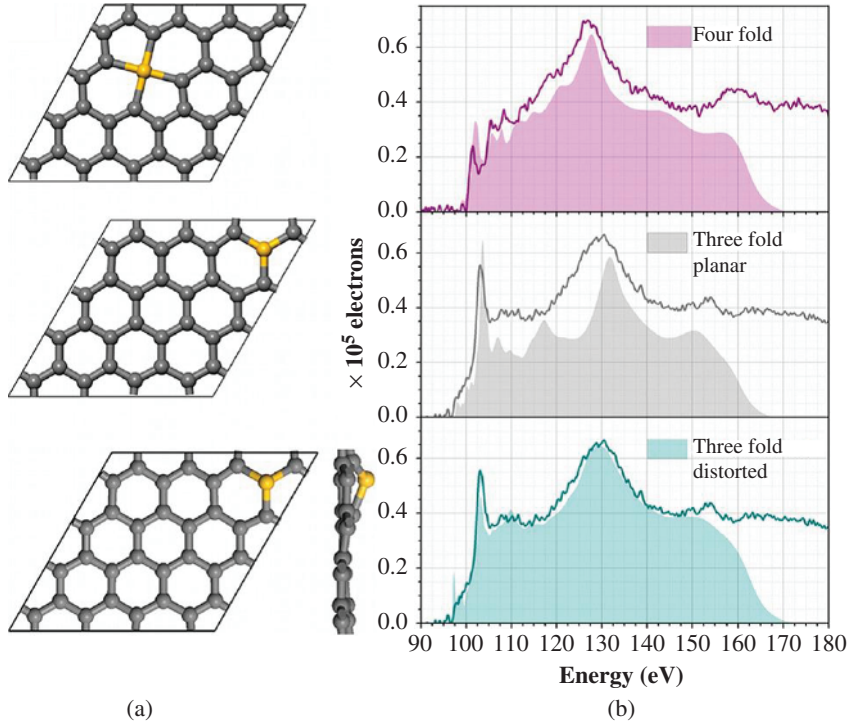

Figure 1.2 (a) Supercells used for simulating the EELS edge shape for fourfold and threefold coordinated silicon dopant atoms in graphene. For the latter, a planar structure and a distorted structure, where the silicon atom is displaced out of the graphene sheet, are assumed. (b) shows the corresponding EELS spectra, with the experimental measurement represented as a solid line and the simulated result superimposed as a filled spectrum. From Ramasse *et al*. (2013). Reproduced with permission; copyright American Chemical Society.

in which it is implemented and consequently the information that can be extracted. For example, if the interest is in images formed from high energy electrons passing through a thin foil, such as in transmission electron microscopy (TEM), then the strongest signal will be due to elastically scattered electrons. The less probable inelastic scattering events can be treated phenomenologically or in certain cases (e.g. a single graphene sheet) ignored altogether. This approach considerably simplifies and speeds up the calculation while still providing the required information.

Four different simulation methods are discussed in this book, namely Monte Carlo (Chapter 2), multislice (Chapter 3), Bloch waves (Chapter 4) and electrodynamic theory (Chapter 6). Chapter 5 deals with inelastic scattering of core atomic electrons and extends the multislice,

Bloch wave methods to include simulation of inelastic images in the form of chemical maps. Together these form a core body of techniques for analysing a large range of electron microscopy data. Electronic structure calculations, based on either density functional theory or multiple scattering, are also widely used for simulating the fine structure of EELS spectra, but are not discussed here in any great detail. This is a vast area separate from the main topic of this book and the interested reader should consult textbooks such as Martin (2004) for further details. Table 1.1 lists some of the advantages and disadvantages of each of the simulation techniques. It should give some indication of which technique to use for a given problem and which techniques to avoid.

Finally, it should be noted that it is impossible to give an exhaustive treatment of electron beam scattering in a book of this size. Instead, the emphasis is on describing the essential physics, so that the reader is able to comprehend a large part of the literature and develop an understanding of simulation packages beyond a mere 'black box'. As for the vast literature on the subject, a word of caution is appropriate: unfortunately, there is no universally accepted notation in scattering theory. In this book, I have tried to be as consistent as possible, following the procedure outlined below:

(i) The relativistic mass of the high energy electron is distinguished from its rest mass by using m for the former and m_o for the latter. There are, however, several examples in the text where the kinetic energy is expressed as $\frac{1}{2}mv^2$, rather than the correct relativistic formula $(\gamma - 1)m_o c^2$, where v is the speed of the electron, c the speed of light and $\gamma = [1 - (v/c)^2]^{-\frac{1}{2}}$. This is standard practice in most of the literature, although for a 300 keV electron beam the fractional error is as large as 18%. The magnitude of the momentum $p = mv$ is, however, relativistically correct, and consequently there is no error in the de Broglie wavelength.

(ii) An electron plane wave is represented as $\exp(2\pi i\mathbf{k}\cdot\mathbf{r})$, with $\mathbf{k}$ being the wave vector and $\mathbf{r}$ the position vector; some texts may use the form $\exp(i\mathbf{k}\cdot\mathbf{r})$. With the notation adopted in this book the integrand of the Fourier transform of a function $f(\mathbf{r})$ is $f(\mathbf{r})\exp(-2\pi i\mathbf{q}\cdot\mathbf{r})$, where $\mathbf{q}$ is the reciprocal space variable.

(iii) The potential energy of an electron in a potential field $V(\mathbf{r})$ is $-eV(\mathbf{r})$, where $-e$ is the charge of the electron. The Schrödinger equation then becomes $[\hbar^2\nabla^2/2\,m + eV(\mathbf{r}) + E]\psi(\mathbf{r}) = 0$, where $\hbar$ is the reduced Planck's constant, E the energy and $\psi(\mathbf{r})$ the electron wavefunction. In some texts, the potential energy is denoted by $V(\mathbf{r})$ and the

Table 1.1 The simulation methods discussed in this book and some of their advantages and disadvantages

Simulation method	Advantages	Disadvantages
Monte Carlo (probabilistic scattering of particles, e.g. incident electrons)	• Both elastic and inelastic scattering are readily incorporated • Applicable for a wide range of specimen geometries (SEM[a] and TEM) • Large range of signals can be simulated (e.g. images, electron beam induced current, X-ray generation, etc.)	• Cannot reproduce channelling or diffraction in a crystal • Inelastic scattering is often modelled as a continuous energy loss (i.e. stopping power). Hence 'straggling' is not observed
Multislice (physical optics approach based on transmission and propagation of the incident electron wave)	• Used in both TEM and STEM image simulations • Channelling and dynamic diffraction in a crystal are reproduced • Supercells can be constructed, such as defects, amorphous materials, etc.	• Most software packages only simulate elastic scattering, with thermal diffuse scattering modelled as a pseudo-elastic scattering event (i.e. frozen phonon). Core level inelastic scattering can be included, but at the expense of computing time • Computing time increases with thickness of the specimen • Can be difficult to interpret the underlying scattering mechanisms

Bloch wave (based on Schrödinger's equation for an electron in a periodic potential)	• Used in both TEM and STEM image simulations • Channelling and dynamic diffraction in a crystal are reproduced • Intuitive description of dynamic diffraction • Computing time does not increase with specimen thickness (unless information at different depths is required)	• Most software packages only simulate elastic scattering, with thermal diffuse scattering modelled phenomenologically via an 'optical potential'. Core level inelastic scattering can be included, but at the expense of computing time • Only useful as a computational technique for periodic crystals with small unit cells. Column approximation and/or perturbation methods can nevertheless be used to obtain useful information about defect crystals
Electrodynamic theory (based on Maxwell's equations)	• Vastly simplifies inelastic scattering events involving many electrons, for example, plasmons • Only the specimen dielectric function is required to calculate the energy loss • Analytical solutions are available for relatively simple specimen geometries (e.g. thin films, spheres, etc.) • Radiative phenomena, such as Cerenkov and transition radiation, can also be analysed	• Only valid when the energy loss is a negligible fraction of the incident electron energy • Simulation methods exist for arbitrary specimen geometries, but can be computationally intensive

[a]Scanning electron microscope.

Schrödinger equation modified accordingly. The term 'potential' is also frequently used to mean 'potential energy', although they are not the same, though closely related. The notation here makes the distinction more transparent.

(iv) The magnitude of the elastic scattering vector is $q = 2\sin\theta/\lambda$, where θ is the scattering semi-angle and λ the electron wavelength. The Debye–Waller factor (B) in the thermal smearing term '$\exp(-Bq^2)$' is then equal to $2\pi^2\overline{x^2}$, where $\overline{x^2}$ is the mean square atom displacement (Chapter 3). The definition $q = \sin\theta/\lambda$ is also sometimes used, in which case, $B = 8\pi^2\overline{x^2}$.

(v) The inelastic scattering vector is $\mathbf{q} = k_m\mathbf{n}_m - k_0\mathbf{n}_0$, where k_0, k_m are wave numbers (see also [ii] for wave vector definition) for the incident and inelastically scattered electron along the unit vector directions $\mathbf{n}_0$ and $\mathbf{n}_m$ respectively. In many texts, $\mathbf{q} = 2\pi[k_m\mathbf{n}_m - k_0\mathbf{n}_0]$. The motivation for using the alternative notation here is that it is consistent with the definition of the elastic scattering vector, but more importantly because the results from quantum mechanics (Chapter 5) can be directly compared with electrodynamics (Chapter 6). The latter frequently uses Fourier transforms, which follow the notation outlined in (ii).

(vi) Maxwell's equations are expressed in SI units. The equivalent expressions in Gaussian units can be found in Jackson (1998).

REFERENCES

Jackson, J.D. (1998) *Classical Electrodynamics*, John Wiley & Sons, New York.

Martin, R.M. (2004) *Electronic Structure- Basic Theory and Practical Methods*, Cambridge University Press, UK.

Moison, J.M., Guille, C., Houzay, F., Barthe, F. and Van Rompay, M. (1989) *Phys. Rev. B* **40**, 6149.

Ramasse, Q.M., Seabourne, C.R., Kepaptsoglou, D.M., Zan, R., Bangert, U. and Scott, A.J. (2013) *Nano Lett.* **13**, 4989.

Robb, P.D. and Craven, A.J. (2008) *Ultramicroscopy* **109**, 61.

Robb, P.D., Finnie, M. and Craven, A.J. (2012) *Ultramicroscopy* **118**, 53.